# Novel 2-benzoyl-3-hydroxy-3-(trifluoromethyl)-3,3a,4,5,6,7-hexahydro-2H-indazole: Synthesis, characterization and computational analysis

Kuvondik G. Avezov [a], Bako B. Umarov [a], Bakhtiyor Sh. Ganiev [a], Raisa B. Zaynieva [b], Gulyayra K. Kholikova [a], Elizaveta V. Panova [c], Damir A. Safin [c,d,*]

[a] *Bukhara State University, M. Ikbol str. 11, Bukhara, 200117, Uzbekistan*
[b] *Bukhara State Technical University, K. Murtazaev str. 15, Bukhara, 200100, Uzbekistan*
[c] *University of Tyumen, Volodarskogo Str. 6, 625003 Tyumen, Russian Federation*
[d] *Department of Technical Sciences, Western Caspian University, Baku, Azerbaijan*

ARTICLE INFO

ABSTRACT

In this work, a novel bicyclic derivative consisting of the fusion of the pyrazoline ring and cyclohexane, namely 2-benzoyl-3-hydroxy-3-(trifluoromethyl)-3,3a,4,5,6,7-hexahydro-2H-indazole (**1**), is reported. Compound **1** was obtained by condensation of 2-trifluoroacetylcyclohexanone with benzohydrazide in the ethanolic medium. The structure of **1** was confirmed through microanalysis, IR spectroscopy and NMR spectroscopy. The structure in a crystalline phase was revealed through single-crystal X-ray diffraction and further characterized in-depth using Hirshfeld surface analysis. As a result, the presence of only one pair of diastereoisomers, namely (3S,3aR)-2-benzoyl-3-hydroxy-3-(trifluoromethyl)-3,3a,4,5,6,7-hexahydro-2H-indazole (**1-3S,3aR**) and (3R,3aS)-2-benzoyl-3-hydroxy-3-(trifluoromethyl)-3,3a,4,5,6,7-hexahydro-2H-indazole (**1-3R,3aS**), was revealed in the crystal. The discussed compound was additionally studied through DFT calculations to elucidate its electronic and structural characteristics. Its biological activity was evaluated in silico to assess potential ADMET properties. Molecular docking simulations revealed that both isomers of **1** exhibit strong inhibitory potential against hemoglobin S (HbS), the protein responsible for sickle cell anemia (SCA), with ligand efficiency scores aligning with established criteria for a promising drug candidate (Hit).

## 1. Introduction

Of five-membered heterocycles, pyrazolines are significant representatives, which structures contain two nearby located nitrogens. Pyrazoline cycles are commonly found in a great library of the corresponding derivatives, which are of importance for agrochemicals and analytical reagents [1,2]. Furthermore, pyrazoline-based compounds have significant pharmacological properties, making them valuable resources for drug development. Pyrazoline derivatives have demonstrated diverse biological activities, including anti-inflammatory [3,4], anticancer [5], antidiabetic [6], antidepressant [7], antitumor [8], immunosuppressive [9] and antibacterial [10] effects.

According to recently reported findings, incorporation of a fluorine atom might change both the reaction's trajectory and the product's biological characteristics [11,12]. To be said, the fluorinated pyrazoles and pyrazolines have been used as antifungal, antibacterial and antifertility agents [13]. Previous publications have thoroughly described a

number of techniques for the synthesis of both non-halogenated [14–22] and trifluoro(chloro)methyl containing [23–40] pyrazoles. These compounds are often prepared by reacting trifluoromethyl containing reagents with hydrazine derivatives [23,24,27,37,40].

The Cambridge Structural Database identified 28 relevant structures for the hydroxy-thrifluoromethyl-aroyl(alkoyl) substituted pyrazolines, of which only one hit was found for the bicyclic derivative consisting of the fusion of the pyrazoline ring and the other ring, namely 2-cyanoacetyl-3-hydroxy-3-(trifluoromethyl)-3,3a,4,5,6,7-hexahydro-2H-indazole (Chart 1) [41,42]. Thus, the synthesis of the pyrazoline derivatives of the latter type is of importance due to their significance as promising candidates for drug development. Notably, the presence of two chiral carbon centers in the structure of the 3-hydroxy-3-(trifluoromethyl)-3,3a,4,5,6,7-hexahydro-2H-indazole core might also be of importance for the efficiency and selectivity of potential drugs.

Guided by these considerations, we have focused on synthesizing a novel bicyclic derivative consisting of the fusion of the pyrazoline ring
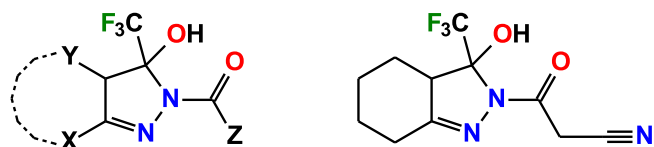
---

* Corresponding author.
*E-mail address:* damir.a.safin@gmail.com (D.A. Safin).

**Chart 1.** (left) A general structure for the hydroxy-thrifluoromethyl-aroyl (alkoyl) substituted pyrazolines revealed in the Cambridge Structural Database; (right) 2-cyanoacetyl-3-hydroxy-3-(trifluoromethyl)-3,3a,4,5,6,7-hexahydro-2*H*-indazole.

and cyclohexane, namely 2-benzoyl-3-hydroxy-3-(trifluoromethyl)-3,3a,4,5,6,7-hexahydro-2*H*-indazole (**1**). Elemental analysis, IR and NMR spectroscopy were employed to characterize the synthesized compound, while single-crystal X-ray diffraction was used to determine its crystal structure, which was further examined through Hirshfeld surface analysis. DFT-based calculations were performed to investigate the compound's electronic and structural properties. Additionally, molecular docking studies were conducted in silico to assess its inhibition potential toward hemoglobin S (HbS), the protein implicated in sickle cell anemia (SCA). This choice was motivated by the structural resemblance between compound **1** and Voxelotor, which is a pyrazole-derived medication currently used to treat SCA, highlighting their shared molecular framework.

## 2. Experimental

### 2.1. Materials and physical measurements

All materials were purchased from commercial suppliers and utilized without additional purification. FTIR spectroscopy was conducted on a Bruker Invenio S-2021 spectrometer using a KBr pellet with spectral data collected at 400–4000 cm$^{-1}$. The NMR spectra were acquired in CD$_3$OD on a JNM-ECZ600R spectrometer. Elemental analysis was carried out with a Carlo Erba EA 1108 elemental analyzer.

### 2.2. Synthesis of 2-benzoyl-3-hydroxy-3-(trifluoromethyl)-3,3a,4,5,6,7-hexahydro-2H-indazole (1)

A solution of 2-trifluoroacetylcyclohexanone (0.01 mol, 1.94 g) in EtOH (20 mL) was combined with a solution of benzohydrazide (0.01 mol, 1.36 g) in the same solvent (30 mL). The mixture was refluxed while monitoring reaction progress via TLC. Upon completion, the crude product precipitated during distillation of approximately two-thirds of the solvent volume. The solid was filtered, washed with EtOH and recrystallized from ethanol to afford the title compound as crystalline material. Yield: 2.06 g (66%). M.p.: 124°C. $^1$H NMR ($\delta_H$): 1.35 (q. t, $^2J_{H,H}$ = 13.3 Hz, $^3J_{H,H}$ = 3.3 Hz, 1H, H5A, CH$_2$, cyclohexane), 1.55 (q. t, $^2J_{H,H}$ = 13.4 Hz, $^3J_{H,H}$ = 3.3 Hz, 1H, H6B, CH$_2$, cyclohexane), 1.72 (q. d, $^2J_{H,H}$ = 13.1 Hz, $^3J_{H,H}$ = 3.4 Hz, 1H, H7B, CH$_2$, cyclohexane), 1.93 (d. m, $^2J_{H,H}$ = 13.4 Hz, 1H, H5B, CH$_2$, cyclohexane), 1.96–2.05 (m, 2H, H6A + H7A, CH$_2$, cyclohexane), 2.30 (t. d. d, $^2J_{H,H}$ = 13.3 Hz, $^3J_{H,H}$ = 6.5 Hz, $^4J_{H,H}$ = 1.3 Hz, 1H, H4B, CH$_2$, cyclohexane), 2.55 (d. d. q, $^2J_{H,H}$ = 29.2 Hz, $^3J_{H,H}$
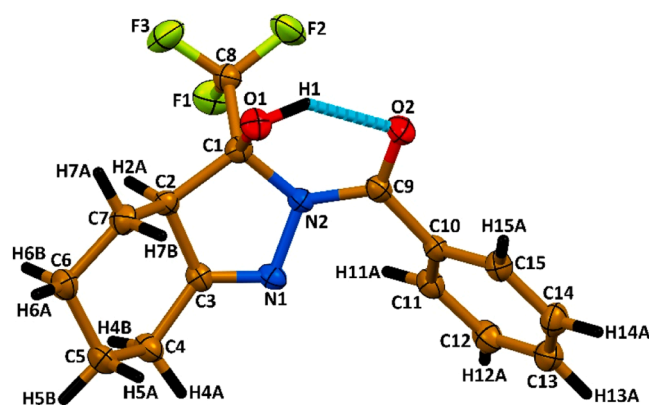


**Fig. 1.** The molecular structure of the **1-3S,3aR** diastereoisomer.

= 14.5 Hz, $^4J_{H,H}$ = 1.6 Hz, 1H, H4A, CH$_2$, cyclohexane), 3.27–3.33 (m, 2H, H2A + H1, cyclohexane + hydroxyl), 7.43 (t. t, $^3J_{H,H}$ = 7.6 Hz, $^4J_{H,H}$ = 1.3 Hz, 2H, H12A + H14A, phenyl), 7.51 (t. t, $^3J_{H,H}$ = 7.5 Hz, $^4J_{H,H}$ = 1.3 Hz, 1H, H13A, phenyl),), 7.72–7.75 (m, 2H, H11A + H15A, phenyl). $^{13}$C{$^1$H} NMR ($\delta_C$): 24.6 (s, C6, CH$_2$, cyclohexane), 26.5 (s, C7, CH$_2$, cyclohexane), 27.0 (s, C5, CH$_2$, cyclohexane), 28.3 (s, C4, CH$_2$, cyclohexane), 53.4 (s, C2, CH, cyclohexane), 92.9 (q, $^2J_{C,F}$ = 33.0 Hz, C1, C (OH)), 125.3 (q, $^1J_{C,F}$ = 285.7 Hz, C8, CF$_3$), 128.8 (s, C12 + C14, CH, Ph), 130.6 (s, C11 + C15, CH, Ph), 132.6 (s, C10, Ph), 135.8 (s, C13, CH, Ph), 162.0 (s, C3, C=N); 171.9 (s, C9, C=O) ppm. Anal. calc. for C$_{15}$H$_{15}$F$_3$N$_2$O$_2$ (312.29) (%): C 57.69, H 4.84 and N 8.97; found: C 57.78, H 4.80 and N 8.91.

### 2.3. Hirshfeld surface analysis

Hirshfeld surface analysis [43–45] was carried out using CrystalExplorer 21 [46] to study the crystal structure.

### 2.4. DFT calculations

The two diastereoisomers of compound **1** were geometry-optimized in gas phase without imposing symmetry constraints using density functional theory (DFT) at the B3LYP/6-311++G(d,p) level [47–49]. Initial structural models for optimization were derived from the experimentally determined crystal geometries of both diastereoisomers. Computational workflows were executed using the GaussView 6.0 visualization interface [50] and the Gaussian 09, Revision D.01 software package [51]. The optimized structures were verified to lack imaginary frequencies through vibrational frequency analysis, ensuring their attainment of energy minima. Additionally, the HOMO, LUMO and MEP surfaces were derived from these optimized geometries.

The "atoms-in-molecules" (AIM) [52] analysis of the electron density, the reduced density gradient (RDG) and non-covalent interactions (NCI) plots [53] were generated using the Multiwfn program [54]. The obtained results from the topological analysis were visualized using the VMD [55] and Gnuplot [56] softwares.
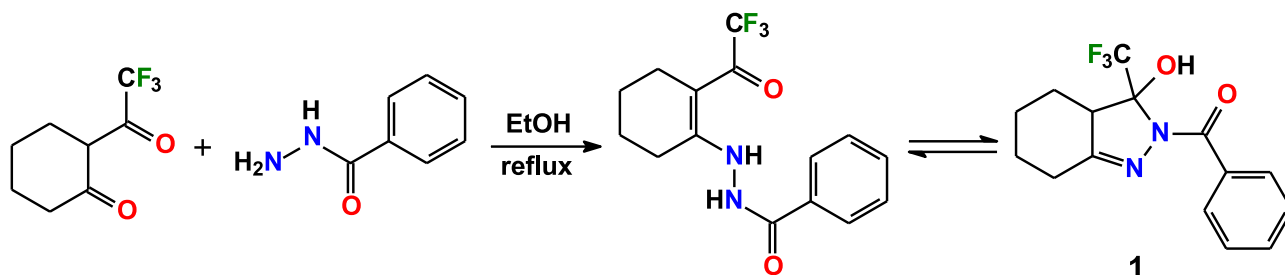


**Scheme 1.** Synthesis of **1**.

**Table 1**

Selected bond lengths (Å) and bond angles (°) in the crystal and optimized structures of **1** (see Figure 1 for atoms labelling).
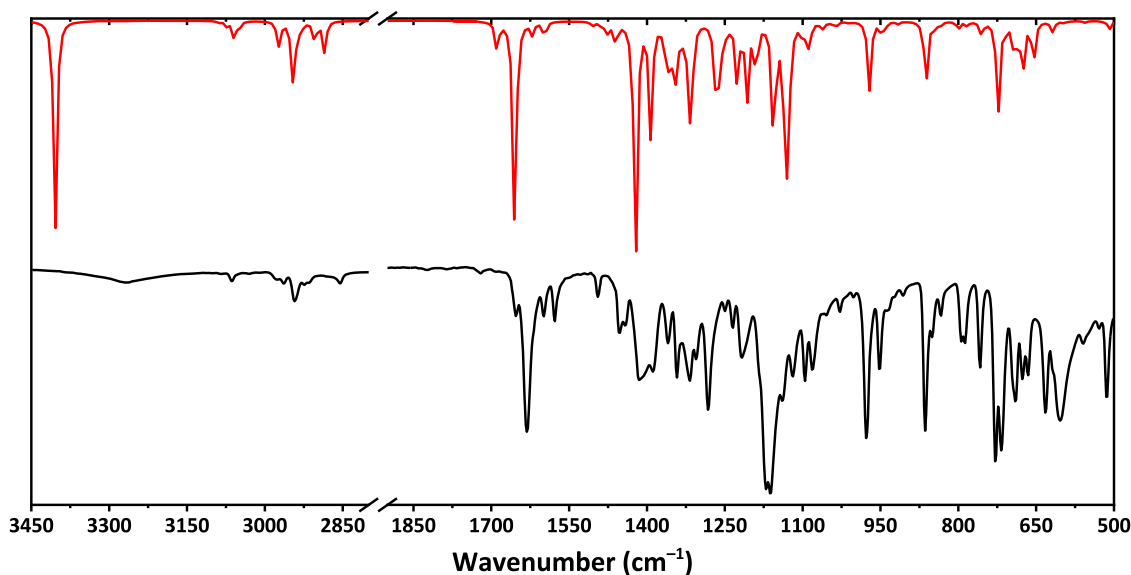
| | Experimental | Optimized | | Experimental | Optimized |
|---|---|---|---|---|---|
| *Bond length* | | | | | |
| N1–N2 | 1.419(3) | 1.404 | C2–C7 | 1.533(3) | 1.540 |
| N1–C3 | 1.273(3) | 1.277 | C3–C4 | 1.488(3) | 1.493 |
| N2–C1 | 1.479(3) | 1.493 | C4–C5 | 1.521(4) | 1.547 |
| N2–C9 | 1.367(3) | 1.384 | C5–C6 | 1.512(4) | 1.537 |
| O1–C1 | 1.396(3) | 1.388 | C6–C7 | 1.523(4) | 1.538 |
| O2–C9 | 1.233(3) | 1.231 | C9–C10 | 1.488(3) | 1.492 |
| F1–C8 | 1.334(3) | 1.354 | C10–C11 | 1.391(3) | 1.400 |
| F2–C8 | 1.318(3) | 1.339 | C10–C15 | 1.389(3) | 1.400 |
| F3–C8 | 1.325(3) | 1.350 | C11–C12 | 1.379(3) | 1.392 |
| C1–C2 | 1.534(3) | 1.554 | C12–C13 | 1.381(4) | 1.394 |
| C1–C8 | 1.527(3) | 1.555 | C13–C14 | 1.374(4) | 1.395 |
| C2–C3 | 1.487(3) | 1.508 | C14–C15 | 1.374(4) | 1.391 |
| *Bond angle* | | | | | |
| N1–N2–C1 | 111.85(16) | 112.21 | C1–N2–C9 | 122.71(17) | 122.13 |
| N1–N2–C9 | 119.85(17) | 121.32 | C1–C2–C3 | 102.21(17) | 101.95 |
| N2–N1–C3 | 107.15(17) | 108.44 | C1–C2–C7 | 117.70(18) | 116.87 |
| N1–C3–C2 | 116.23(19) | 115.37 | C2–C1–C8 | 110.98(17) | 109.79 |
| N1–C3–C4 | 123.6(2) | 124.51 | C2–C3–C4 | 120.04(19) | 119.91 |
| N2–C1–C2 | 102.44(16) | 101.95 | C2–C7–C6 | 108.9(2) | 109.70 |
| N2–C1–C8 | 109.76(17) | 109.16 | C3–C2–C7 | 109.88(17) | 110.43 |
| N2–C9–C10 | 118.78(19) | 119.42 | C3–C4–C5 | 109.8(2) | 109.47 |
| O1–C1–N2 | 113.27(17) | 113.63 | C4–C5–C6 | 112.3(2) | 111.97 |
| O2–C9–N2 | 120.0(2) | 119.51 | C5–C6–C7 | 111.6(2) | 112.17 |
| O1–C1–C2 | 112.06(17) | 112.10 | C9–C10–C11 | 123.11(18) | 123.51 |
| O1–C1–C8 | 108.28(17) | 109.93 | C9–C10–C15 | 117.28(19) | 116.80 |
| O2–C9–C10 | 121.25(19) | 121.06 | C10–C11–C12 | 119.4(2) | 119.97 |
| F1–C8–F2 | 105.85(18) | 107.62 | C10–C15–C14 | 120.3(2) | 120.31 |
| F1–C8–F3 | 106.03(17) | 107.18 | C11–C10–C15 | 119.6(2) | 119.53 |
| F2–C8–F3 | 107.47(17) | 107.56 | C11–C12–C13 | 120.7(2) | 120.27 |
| F2–C8–C1 | 114.18(18) | 113.14 | C12–C13–C14 | 119.8(2) | 119.95 |
| F1–C8–C1 | 111.72(17) | 111.03 | C13–C14–C15 | 120.3(3) | 119.96 |
| F3–C8–C1 | 111.11(18) | 110.06 | | | |

**Table 2**

Hydrogen bond lengths (Å) and angles (°) in the crystal and optimized structures of **1** (see Figure 1 for atoms labelling).

| | D–H···A | d(D–H) | d(H···A) | d(D···A) | ∠(DHA) |
|---|---|---|---|---|---|
| **Experimental** | O1–H1···O2 | 0.94(3) | 1.91(3) | 2.671(3) | 137(2) |
| **Optimized** | | 0.979 | 1.859 | 2.662 | 137.19 |

## 2.5. Molecular docking

Molecular docking simulations were conducted via the CB-Dock2 online platform [57,58], employing the AutoDock Vina algorithm [59]. The HbS protein structure, retrieved from the RCSB Protein Data Bank (PDB ID: 5UFJ) [60], underwent pre-docking preparation, including removal of water and ligands, addition of hydrogen atoms, completion of missing residues, and assignment of appropriate charges.



**Fig. 2.** The experimental IR spectrum of **1** (black) and the calculated IR spectrum of the optimized structure of the **1-3S,3aR** diastereoisomer (red).
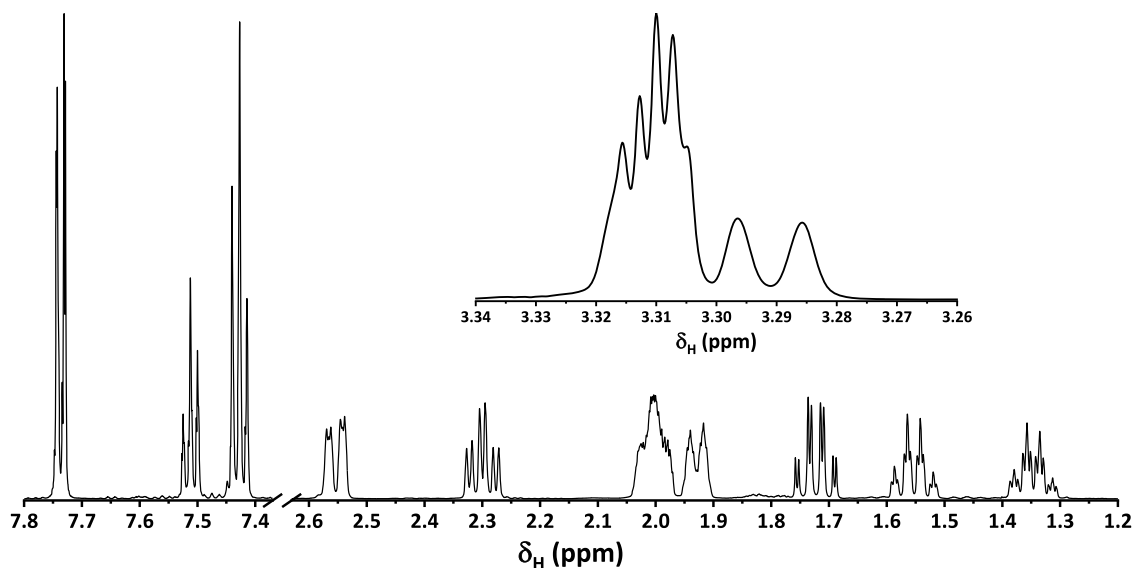
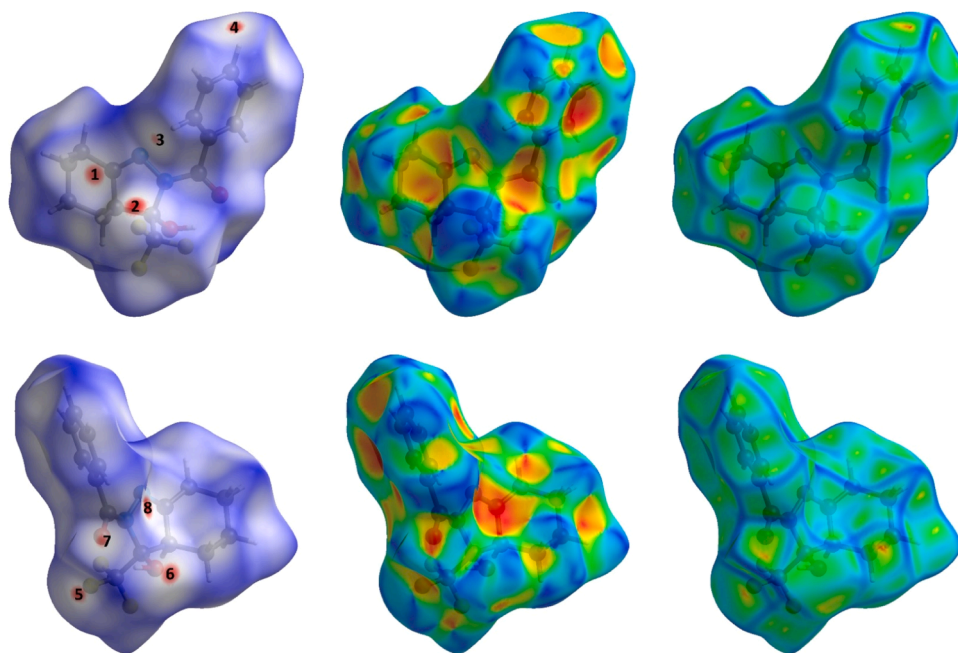**Fig. 3.** The $^1$H NMR spectrum of **1**, recorded in CD$_3$OD.



**Fig. 4.** Front and rear perspectives of the Hirshfeld surfaces of **1** (left, middle and right denote normalized distance $d_{norm}$, shape index and curvedness, respectively). Numbers on the $d_{norm}$ surface: 1 = C⋯O–H, 2 = F⋯C=O, 3 = H⋯O=C, 4 = H⋯F, 5 = F⋯H, 6 = H–O⋯C, 7 = C=O⋯H, 8 = O=C⋯F.

The resulting docking poses were visualized and analyzed using BIOVIA Discovery Studio 2020 [61].

### 2.6. In silico ADMET analysis

The ADMET properties of the discussed compound were evaluated in the SwissADME [62] and ProTox 3.0 [63,64] computational tools to predict its pharmacokinetic and toxicity profiles.

### 2.7. X-ray diffraction analysis

Data collection was performed at 293(2) K on an Oxford Diffraction Xcalibur Ruby CCD diffractometer (Mo-Kα, λ = 0.71073 Å; graphite monochromator). Structural solution and refinement were carried out using SHELXL-2014/7 [65], employing direct methods for solution and full-matrix least-squares for refinement. Non-hydrogen and OH hydrogen atoms were refined with anisotropic displacement parameters, while CH hydrogen atoms were positioned geometrically and modeled as riding atoms with isotropic parameters set to 1.2 those of their carrier atoms. C$_{15}$H$_{15}$F$_3$N$_2$O$_2$, $M_r$ = 312.29 g mol$^{-1}$, orthorhombic, space group *Pbca*, $a$ = 15.289(7), $b$ = 9.996(8), $c$ = 18.491(7) Å, $V$ = 2826(3) Å$^3$, $Z$ = 8, $\rho$ = 1.468 g cm$^{-3}$, $\mu$(Mo-Kα) = 0.125 mm$^{-1}$, $\theta_{min}$ = 2.20°, $\theta_{max}$ = 25.97°, reflections: 2353 collected, 2317 unique, $R_{int}$ = 0.014, $R_1$(all) = 0.0913, $wR_2$(all) = 0.1100, $S$ = 1.016.

CCDC 2443331 contains the crystallographic data. These data can be obtained free of charge via https://www.ccdc.cam.ac.uk/structures or from the Cambridge Crystallographic Data Centre, 12 Union Road, Cambridge CB2 1EZ, UK; fax: (+44)-1223-336-033; or e-mail: deposit@ccdc.cam.ac.uk.
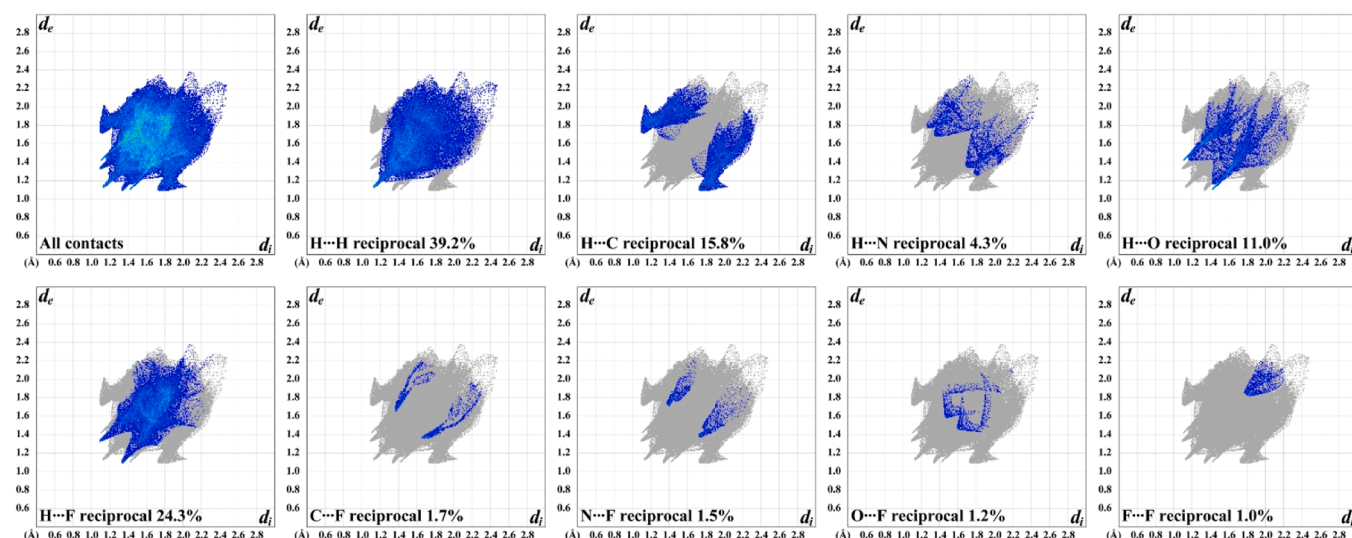
**Fig. 5.** 2D fingerprint plots of the main contacts in the structure of **1**.

**Table 3**
Hirshfeld contact surfaces for **1**, alongside calculated random contact distributions and enrichment ratios.

|  | H | C | N | O | F |
|---|---|---|---|---|---|
| Contacts (*C*, %)[a] |  |  |  |  |  |
| H | 39.2 | – | – | – | – |
| C | 15.8 | 0.0 | – | – | – |
| N | 4.3 | 0.0 | 0.0 | – | – |
| O | 11.0 | 0.0 | 0.0 | 0.0 | – |
| F | 24.3 | 1.7 | 1.5 | 1.2 | 1.0 |
| Surface (*S*, %) |  |  |  |  |  |
|  | 66.9 | 8.8 | 2.9 | 6.1 | 15.4 |
| Random contacts (*R*, %) |  |  |  |  |  |
| H | 44.8 | – | – | – | – |
| C | 11.7 | 0.8 | – | – | – |
| N | 3.9 | 0.5 | 0.1 | – | – |
| O | 8.2 | 1.1 | 0.4 | 0.4 | – |
| F | 20.5 | 2.7 | 0.9 | 1.9 | 2.4 |
| Enrichment (*E*)[b] |  |  |  |  |  |
| H | 0.88 | – | – | – | – |
| C | 1.35 | – | – | – | – |
| N | 1.11 | – | – | – | – |
| O | 1.35 | 0.00 | – | – | – |
| F | 1.18 | 0.63 | – | 0.64 | 0.42 |

[a] Values were derived using the CrystalExplorer 21 software [46].
[b] Enrichment ratios were excluded from calculation when random contacts constituted less than 0.9% of interactions, as these values lack statistical significance [45].

## 3. Results and discussion

A facile condensation reaction of 2-trifluoroacetylcyclohexanone with an equimolar amount of benzohydrazide produced a novel bicyclic derivative consisting of the fusion of the pyrazoline ring and cyclohexane **1** (Scheme 1).

Compound **1** crystallized in the orthorhombic *Pbca* space group, adopting an asymmetric unit containing a single molecule. Interestingly, the structure of **1** contains two chiral carbon centers, namely C1 and C2 (Figure 1) and, thus, the formation of two pairs of diastereoisomers is possible from the synthesis. However, the crystal structure of **1** revealed only one pair of diastereoisomers, namely (3*S*,3a*R*)-2-benzoyl-3-hydroxy-3-(trifluoromethyl)-3,3a,4,5,6,7-hexahydro-2*H*-indazole (**1-3*S*,3a*R***) and (3*R*,3a*S*)-2-benzoyl-3-hydroxy-3-(trifluoromethyl)-3,3a,4,5,6,7-hexahydro-2*H*-indazole (**1-3*R*,3a*S***). Notably, a similar pair of diastereoisomers was previously reveled in the crystal structure of 2-cyanoacetyl-3-hydroxy-3-(trifluoromethyl)-3,3a,4,5,6,7-hexahydro-2*H*-
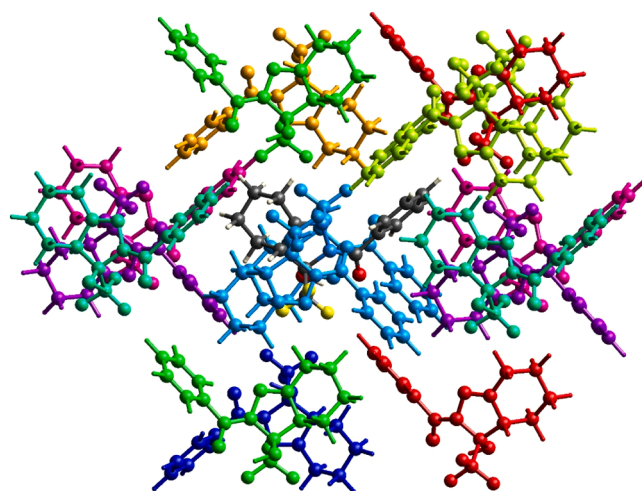


**Fig. 6.** Color-coded intermolecular interaction mapping within a 3.8 Å radius of the central molecule in the crystal structure of **1**, derived from single-point molecular wavefunction calculations at the B3LYP/6-31G(d,p) level.

indazole and it was also reported from the theoretical calculations that the **3*S*,3a*R*** and **3*R*,3a*S*** pair is more stable in comparison to the **3*S*,3a*S*** and **3*R*,3a*R*** pair [41,42]. Thus, a pair of diastereoisomers, where the CF$_3$ functionality and the cyclohexane methine hydrogen atom are *cis*-located, is more favorable (Figure 1).

The N2–C1 and C2–C3 bond lengths within the pyrazoline ring are very similar and of about 1.48 Å, while the N1–N2 and C1–C2 bonds are about 0.06 Å shorter and about 0.05 Å longer, respectively (Table 1). The N1–C3 bond is the shortest one within the same ring and is of about 1.27 Å, indicating its double bond nature (Table 1). Remaining C–C bonds within the cyclohexane ring vary from about 1.49 Å to 1.53 Å, while the same bonds of the phenyl fragment are somewhat shorter and of ~1.37–1.39 Å (Table 1). The C1–C8 bond is about 1.53 Å, while the C9–C10 bond is about 0.04 Å (Table 1), which is due to the formation of the former and the latter bonds by the sp$^3$- and sp$^2$-hybridized carbon atoms, respectively. The C–F bonds are similar and of about 1.32–1.33 Å (Table 1). The C1–O1 bond is about 1.40 Å, while the C9–O2 bond is 0.17 Å shorter due to its double bond nature (Table 1). Finally, all the bond angles formed by the non-H-atoms are of typical values either for the sp$^2$- (111.85(16)–123.11(18)°) or sp$^3$-hybridized atoms (102.21

**Table 4**
Interaction energies (kJ/mol) for the crystal structure of **1**, calculated using the B3LYP/6-31G(d,p) level. Values in parentheses represent normalized attractive energy contributions, expressed as percentages relative to the total attractive interaction energy (scaled to 100%).

| | $N^a$ | Symmetry operation | $R$ | $E_{ele}^b$ | $E_{pol}^b$ | $E_{dis}^b$ | $E_{rep}^b$ | $E_{tot}^b$ |
|---|---|---|---|---|---|---|---|---|
| | 2 | $x + 1/2, y, -z + 1/2$ | 10.22 | −2.8 (21.7) | −0.9 (7.0) | −9.2 (71.3) | 6.0 | −7.9 |
| | 1 | $-x, -y, -z$ | 7.28 | −9.3 (15.6) | −3.0 (5.0) | −47.5 (79.4) | 25.8 | −37.5 |
| | 2 | $-x, y + 1/2, -z + 1/2$ | 10.83 | −2.2 (20.6) | −0.1 (0.9) | −8.4 (78.5) | 3.7 | −7.4 |
| | 2 | $x + 1/2, -y + 1/2, -z$ | 9.07 | −2.8 (20.3) | −0.4 (2.9) | −10.6 (76.8) | 3.9 | −10.1 |
| | 2 | $x, -y + 1/2, z + 1/2$ | 10.16 | 0.4 | −0.5 (5.4) | −8.8 (94.6) | 2.3 | −6.2 |
| | 2 | $-x + 1/2, y + 1/2, z$ | 5.07 | −13.5 (20.2) | −3.7 (5.5) | −49.5 (74.2) | 25.5 | −44.3 |
| | 1 | $-x, -y, -z$ | 8.87 | 1.4 | −0.4 (6.1) | −6.2 (93.9) | 0.1 | −4.2 |
| | 2 | $-x + 1/2, -y, z + 1/2$ | 9.32 | −8.2 (21.9) | −1.7 (4.5) | −27.5 (73.5) | 15.0 | −24.5 |
| | 2 | $x, -y + 1/2, z + 1/2$ | 10.90 | 1.0 | −0.4 (4.2) | −9.2 (95.8) | 3.7 | −5.0 |

[a] $N$ denotes the number of molecules exhibiting a centroid-to-centroid distance $R$ (Å), while the color codes in the first column correlate with the visualization scheme in Figure 6.

[b] $E_{ele}$ is the electrostatic energy, $E_{pol}$ is the polarization energy, $E_{dis}$ is the dispersion energy, $E_{rep}$ is the exchange-repulsion energy, $k$ values are scale factors; $E_{tot} = k_{ele} \times E_{ele} + k_{pol} \times E_{pol} + k_{dis} \times E_{dis} + k_{rep} \times E_{rep} = 1.057 \times E_{ele} + 0.740 \times E_{pol} + 0.871 \times E_{dis} + 0.618 \times E_{rep}$ [66].
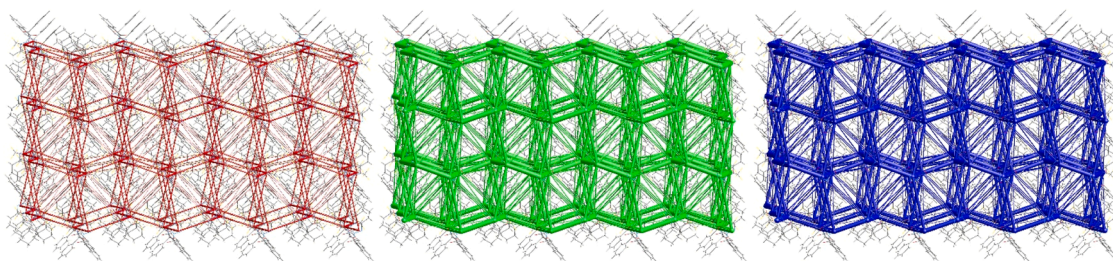


**Fig. 7.** Energy framework diagrams illustrating electrostatic (red), dispersion (green) and total (blue) interaction energies for the crystal structure of compound **1**, calculated using the B3LYP/6-31G(d,p) method. Cylinder diameters correlate with the relative magnitude of energy contributions, normalized to a uniform scale of 100 kJ/mol across a 4 × 2 × 2 unit cell array.

(17)–117.70(18)°) (Table 1).

Stabilization of the molecular structure arises from an O1–H1⋯O2 hydrogen bond linking the hydroxyl hydrogen and carbonyl oxygen atoms, which generates a six-membered ring structure stabilized non-covalently (Figure 1, Table 2).

The experimental FTIR spectrum of **1** exhibits bands at ~2830–3080 cm⁻¹ due to CH stretchings (Figure 2). A broad band at 3270 cm⁻¹ corresponds to the OH group (Figure 2). The C=O and C=N groups were observed as bands at about 1630 and 1655 cm⁻¹, of which the former band is strong, while the C=C vibrations were shown as bands at about 1580 and 1600 cm⁻¹ (Figure 2). The CF groups were found in the spectrum as intense bands at 1165 cm⁻¹ (Figure 2).

The ¹H NMR spectrum of **1**, recorded in CD₃OD, contains two quartet of triplets, one quartet of doublets, one doublet of multiplets, one multiplet, one triplet of doublet of doublets and one doublet of doublet of quartets at 1.35, 1.55, 1.72, 1.93, 1.96–2.05, 2.30 and 2.55 ppm, respectively, corresponding to the cyclohexane CH₂ protons (Figure 3). The phenyl protons were shown in the spectrum as two triplet of triplets and one multiplet at 7.43, 7.51 and 7.72–7.75 ppm, which were attributed to the *meta-*, *para-* and *ortho*-hydrogen atoms, respectively (Figure 3). Finally, the ¹H NMR spectrum also exhibits signals at 3.27–3.33 ppm, which are overlapped with the solvent signal, corresponding to the methine CH and OH protons (Figure 3). The ¹³C{¹H} spectrum of **1**, recorded in the same solvent, exhibits four singlets at 24.6, 26.5, 27.0 and 28.3 ppm, corresponding to the cyclohexane CH₂ carbon atoms, while the methine carbon atom was shown as a singlet at 53.4 ppm. The phenyl carbons were found in the spectrum as four

singlets at 128.8, 130.6, 132.6 and 135.8 ppm. Two quartets at 92.9 and 125.3 ppm were attributed to the C(OH) and CF₃ carbons, respectively, while to singlets at 162.0 and 171.9 ppm were assigned to the C=N and C=O carbon atoms, respectively.

The molecular packing of **1** was analyzed via Hirshfeld surface analysis. The $d_{norm}$-plotted surface revealed eight red spots, of which four spots correspond to the fluorine-based, four spots correspond to the carbonyl-based and two spots correspond to the hydroxyl-based interactions (Figure 4). The shape-index mapped Hirshfeld surface enabled identification of donor and acceptor contact counterparts, visualized as blue and red regions (Figure 4). Furthermore, the curvedness-mapped Hirshfeld surface displayed no flat regions, testifying to the absence of π⋯π stacking (Figure 4).

The 2D fingerprint plots revealed that H⋯X/X⋯H (X = H, C, N, O, F) contacts, collectively accounting for ~95% of interactions, serve as the primary contributors to the molecular surface composition (Figure 5, Table 3). The reciprocal H⋯C contacts, which are shown in the form of clearly defined "wings" (Figure 5) with the shortest $d_e + d_i \approx 2.8$ Å, are of the C–H⋯π nature [44]. The shortest H⋯H interactions appear at $d_e + d_i \approx 2.3$ Å (Figure 5). Reciprocal H⋯O/F contacts manifest as symmetrical spike pairs in the fingerprint plots, with minimum $d_e + d_i \approx 2.5$ and 2.4 Å, respectively (Figure 5). Reciprocal H⋯C/N/O/F interactions are preferentially favored, as evidenced by their enrichment ratios exceeding unity (Table 3), reflecting a higher observed frequency of these contacts across the Hirshfeld surface compared to statistically random distributions. In contrast, H⋯H contacts are disfavored, with an enrichment ratio below unity (0.88), indicating their reduced
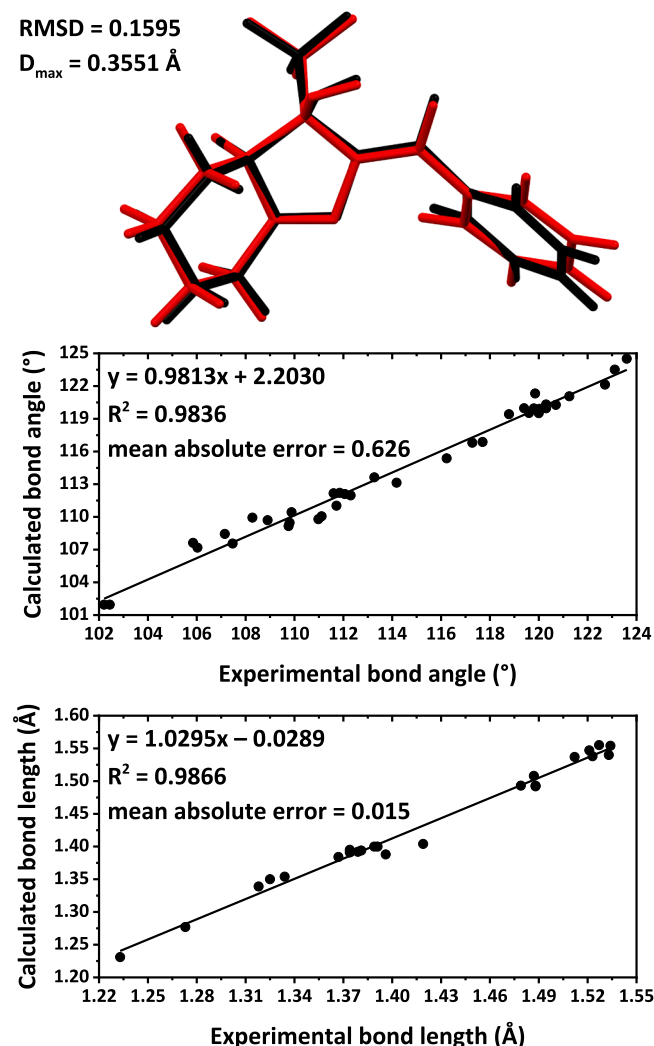
**RMSD = 0.1595**
**D$_{max}$ = 0.3551 Å**



**Fig. 8.** (top) Structural overlay comparing the experimentally determined (black) and computationally optimized (red) molecular geometries of the **1-3S,3aR** diastereoisomer. (bottom) Correlation between the calculated and experimental bond length and bond angle values.

**Table 5**
Dipole moments and descriptors for the optimized structure of the **1-3S,3aR** diastereoisomer.

| | |
|---|---|
| $\mu_D$ (Debye) | 4.8152 |
| $\mu_x$ (Debye) | −0.9283 |
| $\mu_y$ (Debye) | 4.6529 |
| $\mu_z$ (Debye) | 0.8219 |
| $E_{HOMO}$ (eV) | −6.986 |
| $E_{LUMO}$ (eV) | −1.691 |
| $\Delta E_{LUMO-HOMO} = E_{LUMO} - E_{HOMO}$ (eV) | 5.295 |
| Ionization energy, $I = -E_{HOMO}$ (eV) | 6.986 |
| Electron affinity, $A = -E_{LUMO}$ (eV) | 1.691 |
| Electronegativity, $\chi = (I + A)/2$ (eV) | 4.339 |
| Chemical potential, $\mu = -\chi$ (eV) | −4.339 |
| Global chemical hardness, $\eta = (I - A)/2$ (eV) | 2.648 |
| Global chemical softness, $S = 1/(2\eta)$ (eV$^{-1}$) | 0.189 |
| Global electrophilicity index, $\omega = \mu^2/(2\eta)$ (eV) | 3.555 |
| $\Delta N_{max} = -\mu/\eta$ | 1.639 |

prevalence relative to random expectations (Table 3).

A molecular cluster [66] was analyzed to probe energetical properties of intermolecular interactions in **1**. The dispersion energy was found to be the most prevalent component of 71.3–95.8% (Figure 6, Table 4). The frameworks for the corresponding energies [66] are plotted in Figure 7.

Additionally, we used the DFT-based computations to study electronic and structural characteristics of **1**. For structural optimization, we have applied the molecular structure geometries of both isomers **1-3S,3aR** and **1-3R,3aS**. Notably, computations for both isomers produced the same results and, thus, for the purpose of conciseness, we concentrated on the **1-3S,3aR** isomer. The geometrical parameters of the optimized structure are in excellent agreement with the molecular structure of **1-3S,3aR** (Figure 8, Tables 1 and 2).

The **1-3S,3aR** isomer, composed of 37 atoms, exhibits 105 vibrational modes in its IR spectrum. While the calculated spectrum aligns well with the experimental data, notable discrepancies are observed (Figure 2). These differences likely arise from the gas-phase optimization of the isolated isomer, which does not account for solid-state effects (e.g., crystal packing or intermolecular interactions) present in the experimental IR measurements.

The optimized isomer **1-3S,3aR** exhibits a dipole moment of 4.8152 Debye, predominantly governed by its $\mu_y$ component (Table 5). Computational analysis revealed a HOMO energy of −6.986 eV and a LUMO energy of −1.691 eV, yielding an energy gap of 5.295 eV, with ionization energy (6.986 eV) and electron affinity (1.691 eV) values consistent with strong electron-accepting behavior. The compound demonstrates limited propensity for electron cloud exchange with its environment, as indicated by its high chemical hardness ($\eta$) and low chemical softness ($S$) (Table 5). The electrophilicity index ($\omega$) aligns with values characteristic of potent electrophilic species [67]. Additionally, the **1-3S,3aR** isomer displays a maximum electron-accepting capacity of ~1.6 electrons (Table 5).

The HOMO is delocalized on almost the molecule except one of the *ortho-* and the opposite *meta*-CH groups of the phenyl fragments, and the fluorine atoms, while the LUMO is found over the benzoyl and the pyrazoline N2–N1–C3 fragments (Figure 9).

The MEP surface identified the carbonyl oxygen atom as the most nucleophilic regions, followed by the hydroxyl oxygen atom, while the CH$_2$ hydrogen atoms emerged as the most prominent electrophilic sites (Figure 10).

Intramolecular interactions in the optimized structure of the **1-3S,3aR** isomer were examined using the reduced density gradient (RDG) approach. Analysis of the obtained RDG plot revealed a set of high repulsive interactions (Figure 11). Furthermore, a set of weak van der Waals interactions can be revealed on the RDG plot (Figure 11). Notably, the RDG plot also exhibits a spread region at a highly negative side (Figure 11), indicating a notable attraction due to the above mentioned O1–H1⋯O2 hydrogen bond (Figure 1). The combined QTAIM and NCI plot analysis of the optimized structure of the **1-3S,3aR** isomer revealed three bond baths. In particular, a bond path with the corresponding critical point, accompanied with the dark blue RDG isosurface, was found between the hydroxyl hydrogen atom and the carbonyl oxygen atom (Figure 11), yielding the above mentioned O1–H1⋯O2 hydrogen bond (Figure 1). The second bond path with the corresponding critical point, accompanied with the green RDG isosurface, was observed between the same carbonyl oxygen atom and one of the trifluoromethyl fluorine atom, yielding a F⋯O interaction (Figure 11). Finally, the third bond path with the corresponding critical point, accompanied with the green RDG isosurface, was shown between the nitrogen atom of the five-membered ring and one of the *ortho*-hydrogen atoms of the phenyl fragment, yielding a C–H⋯N interaction (Figure 11).

Toxicity profiling of the **1-3S,3aR** isomer was performed using the ProTox 3.0 platform. The compound was classified under Toxicity Class IV (oral administration), with a predicted LD$_{50}$ of 800 mg/kg (Table 6). The same class of toxicity was revealed for paracetamol and erythromycin [68]. Computational toxicity predictions indicate activity in neurotoxicity, ecotoxicity, respiratory toxicity, clinical toxicity and carcinogenicity, while displaying no predicted hepatotoxic, nephrotoxic, cardiotoxic, immunotoxic, cytotoxic or nutritional toxicity (Table 6). Further comparison of the predicted toxicity results of the
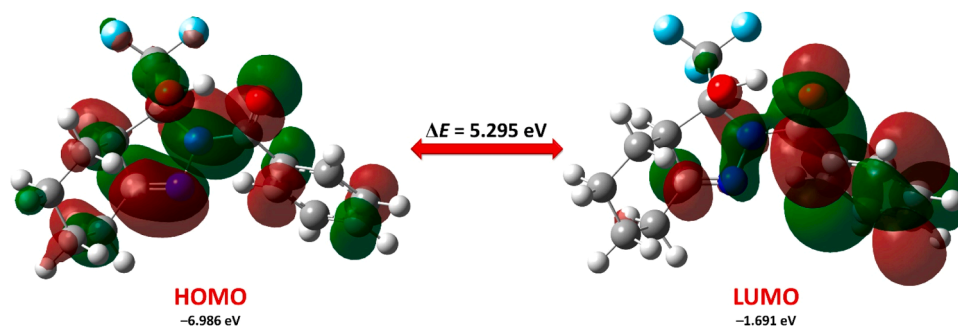
**Fig. 9.** The HOMO and LUMO of the optimized structure of the **1-3S,3aR** diastereoisomer.
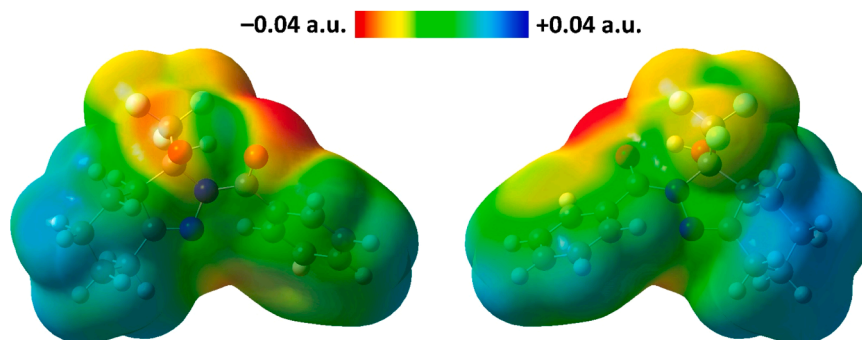


**Fig. 10.** Front and rear perspectives of the MEP surface for the optimized structure of the **1-3S,3aR** diastereoisomer.
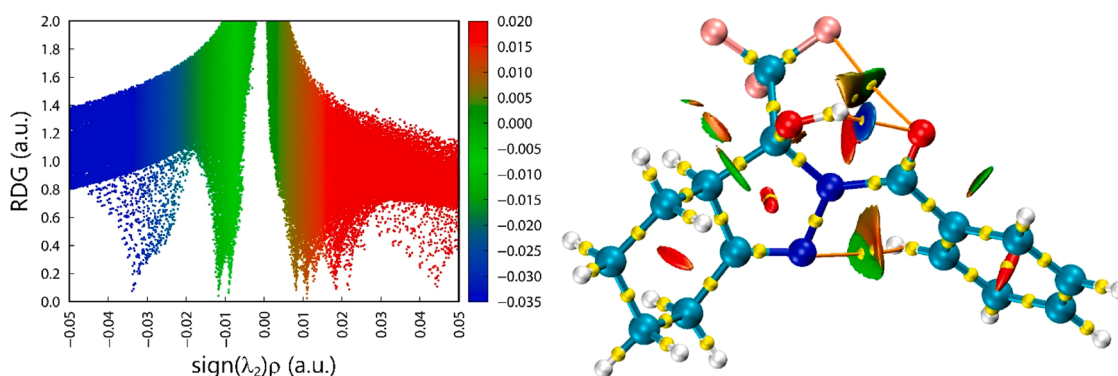


**Fig. 11.** The RDG (left) and QTAIM/NCI (right) plots of the optimized structure of the **1-3S,3aR** diastereoisomer. Bond critical points and bond paths in the QTAIM/NCI plot are shown as small yellow spheres and orange lines, respectively.

**1-3S,3aR** isomer with Paracetamol and Erythromycin, which are known hepatotoxic agents, and with Acetylcysteine, which is a known hepatoprotective agent [69], revealed that the reported herein compound is much less hepatotoxic than Paracetamol and Erythromycin but slightly more hepatotoxic than Acetylcysteine as well as Cyclophosphamide and Doxorubicin (Table 6) [68]. Furthermore, the **1-3S,3aR** isomer is predicted to be less carcinogenic than Cyclophosphamide but much more carcinogenic than Paracetamol, Erythromycin, Acetylcysteine and Doxorubicin (Table 6) [68]. The same isomer is as highly inactive in immunotoxicity as Paracetamol, Cyclophosphamide and Acetylcysteine, while less mutagenic and cytotoxic in comparison to Paracetamol and Erythromycin (Table 6) [68].

The bioavailability radar analysis indicates that **1-3S,3aR** satisfies all six pharmacokinetic criteria, with predicted inhibitory activity against nuclear receptors, enzymes, kinases, proteases, family B G protein-coupled receptors, voltage-gated ion channels, reader and ligand-gated ion channels (Figure 12). The BOILED-Egg model predicts high blood-brain barrier (BBB) permeability and gastrointestinal (GI) absorption

for the compound, while suggesting negligible P-glycoprotein-mediated efflux from the central nervous system (Figure 12).

Sickle cell anemia (SCA) is a severe genetic blood disorder and one of the most widespread inherited diseases globally. First emerging in Africa, SCA has since spread across continents through human migration over centuries [70,71]. Over 300000 newborns globally are estimated to have this disease each year [72]. It is caused by a mutation on human chromosome 11 where thymine replaces adenine [71]. The β-globin gene mutation involves a single nucleotide substitution (GAG → GTG), replacing the hydrophilic glutamic acid with hydrophobic valine at position six of the β-globin subunit. This substitution drives hemoglobin S (HbS) polymerization under hypoxic conditions, inducing the characteristic sickle-shaped deformation of red blood cells.

For the purpose of avoiding and reducing problems related to SCA, the US FDA has identified four therapy options: Voxelotor, hydroxyurea, crizanlizumab and L-glutamine [73]. Although the treatment of SCA has greatly improved because to these drugs, researchers are always pushing the envelope to enhance patient outcomes and treatment efficacy.
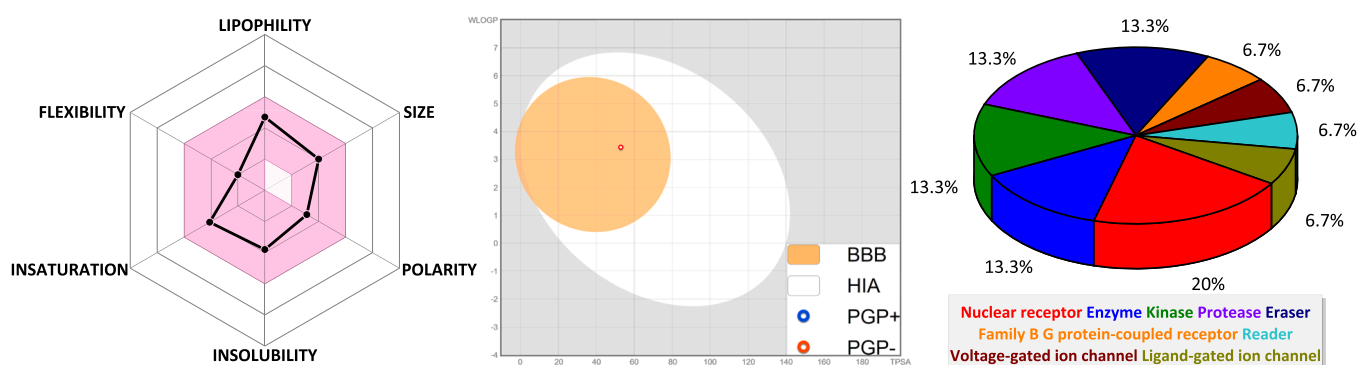
**Table 6**

Toxicity profiling of the **1-3S,3aR** diastereoisomer, obtained from the ProTox 3.0 tool generated toxicity model report and oral toxicity prediction. Toxicity endpoint activities (active/inactive) were classified based on probability scores ranging from 0 to 1.

| Toxicity Model Report | | | |
|---|---|---|---|
| **Target** | **Prediction (Probability)** | **Target** | **Prediction (Probability)** |
| Hepatotoxicity | Inactive (0.60) | Immunotoxicity | Inactive (0.97) |
| Neurotoxicity | Active (0.70) | Mutagenicity | Inactive (0.58) |
| Nephrotoxicity | Inactive (0.56) | Cytotoxicity | Inactive (0.63) |
| Respiratory toxicity | Active (0.67) | Ecotoxicity | Active (0.57) |
| Cardiotoxicity | Inactive (0.69) | Clinical toxicity | Active (0.58) |
| Carcinogenicity | Active (0.57) | Nutritional toxicity | Inactive (0.61) |
| **Oral Toxicity Prediction Results** | | | |
| Predicted LD$_{50}$ (mg/kg) | 800 | Average similarity (%) | 48.77 |
| Predicted Toxicity Class | 4 | Prediction accuracy (%) | 54.26 |

Investigating new therapeutic chemicals is a crucial field of research that might eventually result in a better quality of life and a lighter load of difficulties for more SCA patients. With all this in mind, we have in silico probed both isomers of the title compound **1** to inhibit HbS. Notably, one of the mentioned medications, namely Voxelotor, is a pyrazole derivative. Thus, the studied herein compound **1**, which also can be considered as a pyrazole derivative, is worthy to be probed as a potential inhibitor of HbS.

It was established that both isomers of **1** inhibit HbS with the **1-3S,3aR** isomer being slightly more active (Table 7). Complex of HbS with **1-3S,3aR** is due to one carbon hydrogen bond with HIS92; one halogen interaction with HIS92; one π···σ interaction with LEU141; four alkyl interactions with LEU28, VAL67, LEU106 and VAL98; and six π···alkyl interactions with PHE42, HIS63, HIS92, PHE103, VAL67 and ALA70 (Figure 13, Table 8). Complex HbS–**1-3R,3aS** is characterized by one carbon hydrogen bond with HIS92; one halogen interaction with ASN102; two alkyl interactions with LEU31 and LEU106; and five π···alkyl interactions with PHE42, HIS92, VAL67, ALA70 and LEU141 (Figure 13, Table 8). Interestingly, although the studied compound **1**

comprises a carbonyl oxygen atom, either isomers do not form interactions with the HbS protein due to this functionality (Figure 13, Table 8), which is, in turn, known as a pronounced hydrogen bond promoter. Instead, both isomers form a halogen interaction due to one of the fluorine atoms (Figure 13, Table 8). Furthermore, the second fluorine atom of the **1-3S,3aR** isomer and the hydroxyl oxygen atom of the **1-3S,3aS** isomer are involved in the formation of the carbon hydrogen bonds with HbS (Figure 13, Table 8). Finally, both the cyclohexane and phenyl fragments are responsible for the formation of hydrophobic interactions with the HbS protein (Figure 13, Table 8). Contrarily, the formation of complex of HbS with Voxelotor is exclusively characterized by the formation of hydrophobic interactions. In particular, complex HbS–Voxelotor is described by two π···σ interactions with VAL67 and LEU106; two π···π T-shaped interactions with PHE42 and HIS92; and seven π···alkyl interactions with PHE42, LEU28, VAL67, ALA70, LEU88, VAL98 and LEU106 (Table 8). Notably, although Voxelotor comprises the aldehyde, hydroxyl and ester oxygen atoms as well as the pyridine and pyrazole nitrogen atoms, not a single hydrogen bonding was revealed within the interactions of this molecule with HbS (Table 8).



**Fig. 12.** The bioavailability radar (left), the BOILED-Egg model (middle) and prediction of druggability (right) for the **1-3S,3aR** diastereoisomer.

**Table 7**

Ligand efficiency scores for complexes of **1-3S,3aR, 1-3R,3aS** and Voxelotor with HbS. Docking center (*x, y, z*) = –18, 12, 26; docking size (*x, y, z*) = 20, 26, 26; cavity volume = 1291 Å³.

| Ligand efficiency scores | 1-3S,3aR | 1-3R,3aS | Voxelotor |
|---|---|---|---|
| Binding energy (BE, kcal/mol) | –9.7(1) | –9.4(1) | –8.2(0) |
| Inhibition constant ($K_i = e^{(BE/RT)}$, μM) | 0.078 | 0.129 | 0.993 |
| miLogP (Molinspiration octanol-water partition coefficient) | 3.27 | 3.27 | 2.94 |
| Ligand efficiency (LE = –BE/(Heavy atoms), kcal/(mol HA)) | 0.441 | 0.427 | 0.328 |
| LE_Scale ($0.0715 + 7.5328/(HA) + 25.7079/(HA^2) – 361.4722/(HA^3)$) | 0.433 | 0.433 | 0.391 |
| Fit quality (FQ = LE/LE_Scale) | 1.018 | 0.986 | 0.839 |
| Ligand-efficiency-dependent lipophilicity (LELP = miLogP/LE) | 7.415 | 7.658 | 8.963 |
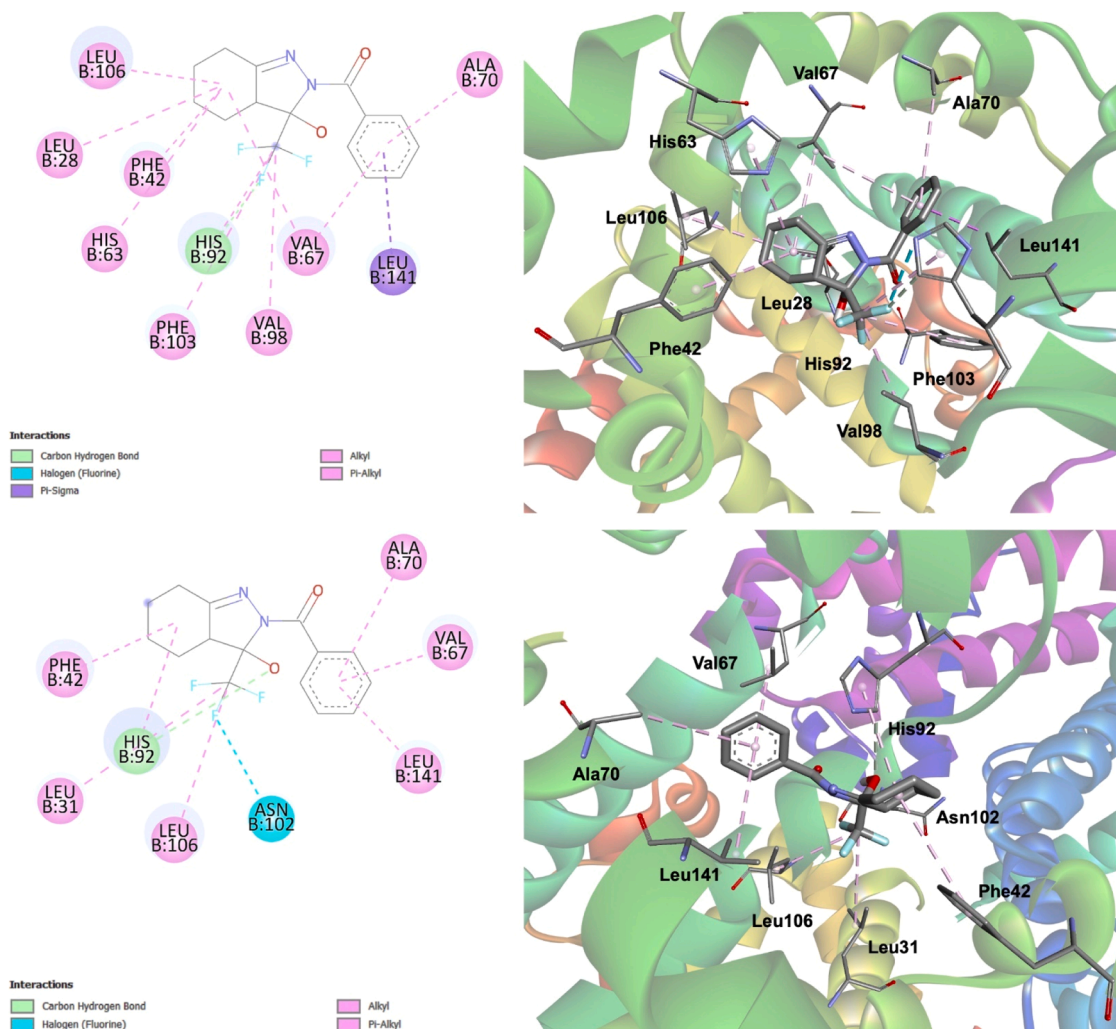
**Fig. 13.** Interaction of HbS with **1-3S,3aR** (top) and **1-3R,3aS** (bottom).

Instead, the benzene, pyridine and pyrazole π-systems are the contributors to the interactions responsible for the binding of Voxelotor with HbS (Table 8).

To assess the potential bioactivity of both isomers of **1** against HbS, we calculated ligand efficiency scores [74–79]. For classification as a Hit, criteria include: $K_i$ between 0.1–1 μM (values <10 nM qualify as drug-like) [78], LE ≥ 0.3, FQ ≥ 0.8 and LELP between −10 and 10 [78]. For both HbS–**1** isomer complexes, all ligand efficiency scores fell within the Hit threshold range (Table 7), suggesting strong potential for therapeutic targeting. Notably, the same scores calculated for Voxelotor revealed its significant inferior activity against HbS in comparison to both isomers of **1** (Table 7). This might be explained by the exclusive formation of hydrophobic interactions between Voxelotor and HbS, while hydrogen and halogen bonds were additionally revealed in complexes of both isomers of **1** with HbS (Table 8).

## 3. Conclusions

A novel bicyclic derivative consisting of the fusion of the pyrazoline ring and cyclohexane, namely 2-benzoyl-3-hydroxy-3-(trifluoromethyl)-3,3a,4,5,6,7-hexahydro-2H-indazole (**1**), which was readily synthesized by a one-pot reaction of 2-trifluoroacetylcyclohexanone with an

equimolar amount of benzohydrazide in the ethanolic medium, is reported. Compound **1** was proved by the means of elemental analysis data, IR, ^{1}H and ^{13}C{^{1}H} NMR spectroscopy. The crystal structure of **1** was elucidated by single crystal X-ray diffraction, which revealed the presence of only one pair of diastereoisomers, namely (3S,3aR)-2-benzoyl-3-hydroxy-3-(trifluoromethyl)-3,3a,4,5,6,7-hexahydro-2H-indazole (**1-3S,3aR**) and (3R,3aS)-2-benzoyl-3-hydroxy-3-(trifluoromethyl)-3,3a,4,5,6,7-hexahydro-2H-indazole (**1-3R,3aS**). Hirshfeld surface analysis of the crystal structure of compound **1** identified reciprocal intermolecular H···X (X = H, C, N, O, F) contacts as the primary contributors to its molecular surface interactions. Structural and electronic properties of the compound were further investigated through the DFT calculations. Both diastereoisomers yielded identical computational results; consequently, only the **1-3S,3aR** isomer was analyzed in detail to streamline the discussion. The optimized structure of **1-3S,3aR** was found to be in excellent agreement with its molecular structure. Analysis of global chemical reactivity parameters and the MEP surface revealed that **1-3S,3aR** exhibits strong electrophilic character. The carbonyl and hydroxyl oxygen atoms serve as the primary nucleophilic sites, while the $CH_2$ hydrogen atoms are identified as the most prominent electrophilic centers.

In silico ADMET profiling classifies **1** under Toxicity Category IV,

**Table 8**

Interactions in complexes of HbS with **1-3S,3aR, 1-3R,3aS** and Voxelotor.

| Interaction | Distance (Å) | Bonding | Bonding type |
|---|---|---|---|
| HbS–**1-3S,3aR** | | | |
| B:HIS92:CD2 – A:**1-3S,3aR**:F2 | 2.754 | Hydrogen bond | Carbon hydrogen bond |
| B:HIS92:NE2 – A:**1-3S,3aR**:F2 | 3.611 | Halogen | Halogen (fluorine) |
| B:LEU141:CD2 – A:**1-3S,3aR** | 3.689 | Hydrophobic | π⋯σ |
| B:LEU28 – A:**1-3S,3aR** | 5.286 | Hydrophobic | Alkyl |
| B:VAL67 – A:**1-3S,3aR** | 4.771 | Hydrophobic | Alkyl |
| B:LEU106 – A:**1-3S,3aR** | 4.680 | Hydrophobic | Alkyl |
| A:**1-3S,3aR**:C8 – B:VAL98 | 4.119 | Hydrophobic | Alkyl |
| B:PHE42 – A:**1-3S,3aR** | 5.198 | Hydrophobic | π⋯Alkyl |
| B:HIS63 – A:**1-3S,3aR** | 5.483 | Hydrophobic | π⋯Alkyl |
| B:HIS92 – A:**1-3S,3aR**:C8 | 4.938 | Hydrophobic | π⋯Alkyl |
| B:PHE103 – A:**1-3S,3aR**:C8 | 4.993 | Hydrophobic | π⋯Alkyl |
| A:**1-3S,3aR** – B:VAL67 | 5.383 | Hydrophobic | π⋯Alkyl |
| A:**1-3S,3aR** – B:ALA70 | 5.102 | Hydrophobic | π⋯Alkyl |
| HbS–**1-3R,3aS** | | | |
| B:HIS92:CD2 – A:**1-3R,3aS**:O1 | 3.746 | Hydrogen bond | Carbon hydrogen bond |
| B:ASN102:O – A:**1-3R,3aS**:F2 | 3.246 | Halogen | Halogen (fluorine) |
| A:**1-3R,3aS**:C8 – B:LEU31 | 4.981 | Hydrophobic | Alkyl |
| A:**1-3R,3aS**:C8 – B:LEU106 | 4.214 | Hydrophobic | Alkyl |
| B:PHE42 – A:**1-3R,3aS** | 5.082 | Hydrophobic | π⋯Alkyl |
| B:HIS92 – A:**1-3R,3aS** | 4.465 | Hydrophobic | π⋯Alkyl |
| A:**1-3R,3aS** – B:VAL67 | 5.117 | Hydrophobic | π⋯Alkyl |
| A:**1-3R,3aS** – B:ALA70 | 5.187 | Hydrophobic | π⋯Alkyl |
| A:**1-3R,3aS** – B:LEU141 | 4.393 | Hydrophobic | π⋯Alkyl |
| HbS–**Voxelotor** | | | |
| B:VAL67:CG1 – A:**Voxelotor** | 3.558 | Hydrophobic | π⋯σ |
| B:LEU106:CD2 – A:**Voxelotor** | 3.829 | Hydrophobic | π⋯σ |
| B:PHE42 – A:**Voxelotor** | 5.214 | Hydrophobic | π⋯π T-shaped |
| B:HIS92 – A:**Voxelotor** | 4.628 | Hydrophobic | π⋯π T-shaped |
| B:PHE42 – A:**Voxelotor**:C17 | 4.611 | Hydrophobic | π⋯Alkyl |
| A:**Voxelotor** – B:LEU28 | 4.859 | Hydrophobic | π⋯Alkyl |
| A:**Voxelotor** – B:VAL67 | 4.651 | Hydrophobic | π⋯Alkyl |
| A:**Voxelotor** – B:ALA70 | 4.848 | Hydrophobic | π⋯Alkyl |
| A:**Voxelotor** – B:LEU88 | 5.278 | Hydrophobic | π⋯Alkyl |
| A:**Voxelotor** – B:VAL98 | 4.837 | Hydrophobic | π⋯Alkyl |
| A:**Voxelotor** – B:LEU106 | 5.116 | Hydrophobic | π⋯Alkyl |

with predicted neurotoxic, ecotoxic, respiratory toxic, clinical toxic and carcinogenic activities. Conversely, the compound shows no hepatotoxic, nephrotoxic, cardiotoxic, immunotoxic, cytotoxic or nutritional toxicity risks. Pharmacokinetically, it exhibits favorable BBB penetration and GA, with negligible P-glycoprotein-mediated efflux from the central nervous system. Molecular docking simulations suggest both isomers of **1** act as potent inhibitors of hemoglobin S, which is the pathogenic driver of sickle cell anemia, with ligand efficiency scores aligning with established criteria for a Hit in drug discovery. The obtained ligand efficiency scores surpassed those of Voxelotor, which is a current sickle cell anemia therapeutic.

## CRediT authorship contribution statement

**Kuvondik G. Avezov:** Methodology, Investigation, Formal analysis, Data curation. **Bako B. Umarov:** Methodology, Investigation, Formal analysis, Data curation. **Bakhtiyor Sh. Ganiev:** Investigation, Formal analysis, Data curation. **Raisa B. Zaynieva:** Investigation, Formal analysis. **Gulyayra K. Kholikova:** Investigation, Formal analysis, Data curation. **Elizaveta V. Panova:** Data curation, Formal analysis, Investigation. **Damir A. Safin:** Writing – review & editing, Writing – original draft, Visualization, Validation, Software, Investigation.

## Declaration of competing interest

The authors declare that they have no known competing financial interests or personal relationships that could have appeared to influence the work reported in this paper.

## Data availability

Data will be made available on request.

## References

[1] R. Mulder, K. Wellinga, J.J. van Daalen, A new class of insecticides, Naturwissenschaften 62 (1975) 531–532.

[2] A.R. Katritzky, C.W. Rees, E.F.V. Scriven, Comprehensive Heterocyclic Chemistry II, Vol. 3, Pergamon Press, Elsevier Science, Ltd., Tarrytown, NY, 1996.

[3] E. Bansal, V.K. Srivastava, A. Kumar, Synthesis and anti-inflammatory activity of 1-acetyl-5-substitute daryl-3-(β-aminonaphthyl)-2-pyrazolines and β-(substitute daminoethyl) amidonaphthalenes, Eur. J. Med. Chem. 36 (2001) 81–92.

[4] F.R. Souza, V.T. Souza, V. Ratzlaff, L.P. Borges, M.R. Oliveira, H.G. Bonacorso, N. Zanatta, M.A.P. Martins, C.F. Mello, Hypothermic and antipyretic effects of 3-methyl- and 3-phenyl-5-hydroxy-5-trichloromethyl-4,5-dihydro-1H-pyrazole-1-carboxyamides in mice, Eur. J. Pharmacol. 451 (2002) 141–147.

[5] F. Manna, F. Chimenti, R. Fioravanti, A. Bolasco, D. Secci, P. Chimenti, C. Ferlini, G. Scambia, Synthesis of some pyrazole derivatives and preliminary investigation of their affinity binding to P-glycoprotein, Bioorg. Med. Chem. Lett. 15 (2005) 4632–4635.

[6] J.H. Ahn, H.-M. Kim, S.H. Jung, S.K. Kang, K.R. Kim, S.D. Rhee, S.-D. Yang, H. G. Cheon, S.S. Kim, Synthesis and DP-IV inhibition of cyano-pyrazoline derivatives as potent anti-diabetic agents, Bioorg. Med. Chem. Lett. 14 (2004) 4461–4465.

[7] Y.R. Prasad, A.L. Rao, L. Prasoona, K. Murali, P.R. Kumar, Synthesis and antidepressant activity of some 1,3,5-triphenyl-2-pyrazolines and 3-(2″-hydroxy naphthalen-1″-yl)-1,5-diphenyl-2-pyrazolines, Bioorg. Med. Chem. Lett. 15 (2005) 5030–5034.

[8] E.C. Taylor, H.H. Patel, Synthesis of pyrazolo[3,4-d]pyrimidine analogues of the potent agent N-{4-[2-(2-amino-4(3H)-oxo-7H-pyrrolo[2,3-d]pyrimidin-5-yl) ethylbenzoyl}-L-glutamic acid (LY231514), Tetrahedron 48 (1992) 8089–8100.

[9] J.G. Lombardino, I.G. Otterness, Novel immunosuppressive agents. Potent immunological activity of some benzothiopyrano[4,3-c]pyrazol-3-ones, J. Med. Chem. 24 (1981) 830–834.

[10] B.S. Holla, P.M. Akberali, M.K. Shivananda, Studies on arylfuran derivatives: Part X. Synthesis and antibacterial properties of arylfuryl-Δ²-pyrazolines, Il Farmaco 55 (2000) 256–263.

[11] B.K. Park, N.R. Kitteringham, P.M. O'Neill, Metabolism of fluorine-containing drugs, Annu. Rev. Pharmacol. Toxicol. 41 (2001), 443–.

[12] A. Strunecká, J. Patoáka, P. Connett, Fluorine in medicine, J. Appl. Biomed. 2 (2004) 141–150.

[13] S.P. Sachchar, A.K. Singh, Synthesis of Some New Fluorinated Heteroaryl Pyrazolines and Isooxazolines as Potential Biocidal Agents, J. Ind. Chem. Soc. 62 (1986) 142–146.

[14] A.N. Kost, I.I. Grandberg, Progress in pyrazole chemistry, Adv. Heterocycl. Chem. 6 (1966) 347–429.

[15] J. Bohrisch, M. Pätzel, C. Mügge, J. Liebscher, Ring Transformation by Ring Chain Transfer VI1: Regioselective Synthesis of (ω-Aminoalkyl)pyrazoles from Semicyclic 3-Chloro-2-propeniminium Salts and Hydrazines, Synthesis (1991) 1153–1156.

[16] X.-j. Wang, J. Tan, K. Grozinger, Cross-coupling of 1-aryl-5-bromopyrazoles: regioselective synthesis of 3,5-disubstituted 1-arylpyrazoles, Tetrahedron Lett 41 (2000) 4713–4716.

[17] Y.R. Huang, J.A. Katzenellenbogen, Regioselective synthesis of 1,3,5-triaryl-4-alkylpyrazoles: novel ligands for the estrogen receptor, Org. Lett. 2 (2000) 2833–2836.

[18] A.R. Katrizky, M. Wang, S. Zhang, M.V. Voronkov, P.J. Steel, Regioselective Synthesis of Polysubstituted Pyrazoles and Isoxazoles, J. Org. Chem. 66 (2001) 6787–6791.

[19] N. Haddad, J. Baron, Novel application of the palladium-catalyzed *N*-arylation of hydrazones to a versatile new synthesis of pyrazoles, Tetrahedron Lett 43 (2002) 2171–2173.

[20] V.K. Aggarwal, J. de Vicente, R.V. Bonnert, A novel one-pot method for the preparation of pyrazoles by 1,3-dipolar cycloadditions of diazo compounds generated in situ, J. Org. Chem. 68 (2003) 5381–.

[21] K.Y. Lee, J.M. Kim, J.N. Kim, Regioselective synthesis of 1,3,4,5-tetrasubstituted pyrazoles from Baylis–Hillman adducts, Tetrahedron Lett 44 (2003) 6737–6740.

[22] S.V. Druzhinin, E.S. Balenkova, V.G. Nenajdenko, Recent advances in the chemistry of α,β-unsaturated trifluoromethylketones, Tetrahedron 63 (2007) 7753–7808.

[23] R. Huisgen, 1,3-Dipolar Cycloadditions. Past and Future, Angew. Chem. Int. Ed. 2 (1963) 565–598.

[24] Y. Nakano, M. Hamaguchi, T. Nagai, A synthetic route to bicyclic pyrazolenines via 3-chloropyrazolines and the ring opening of pyrazolenines to diazoalkenes, J. Org. Chem. 54 (1989) 5912–5919.

[25] R.J. Linderman, K.S. Kirollos, An efficient method for the synthesis of trifluoromethyl substituted heterocycles, Tetrahedron Lett 30 (1989) 2049–2052.

[26] B.C. Hamper, Regioselective synthesis of 1-methyl-3-hydroxy-5-perfluoroalkyl-pyrazoles by the addition of methylhydrazine to perfluoroalkylacetylenic esters, J. Fluorine Chem. 48 (1990) 123–131.

[27] M.E. Jung, I.D. Trifunovich, Efficient synthesis of 2′,3′-dideoxynucleosides and 2′,3′-dideoxy C-nucleosides from D-glucosamine, Tetrahedron Lett 33 (1992) 2921–2924.

[28] M.E.F. Braibante, G.C. Colla, M.A.P. Martins, Haloacetylated enol ethers. 2†. Synthesis of 5-trifluoromethylpyrazoles, J. Heterocycl. Chem. 30 (1993) 1159–1160.

[29] X.-Q. Tang, C.-M. Hu, A novel and practical method for the synthesis of 3-tri-fluoromethylated pyrazoles, Chem. Commun. (1994) 631–632.

[30] X.-Q. Tang, C.-M. Hu, Synthesis of 3-perfluoroalkyl-, including 3-trifluoromethyl-, substituted pyrazoles from perfluoroalkylacetylenes, J. Fluorine Chem. 73 (1995) 129–131.

[31] T.D. Penning, J.J. Talley, S.R. Bertenshaw, J.S. Carter, P.W. Collins, S. Docter, M. J. Graneto, L.F. Lee, J.W. Malecha, J.M. Miyashiro, R.S. Rogers, D.J. Rogier, S. S. Yu, G.D. Anderson, E.G. Burton, J.N. Cogburn, S.A. Gregory, C.M. Koboldt, W. E. Perkins, K. Seibert, A.W. Veenhuizen, Y.Y. Zhang, P.C. Isakson, Synthesis and Biological Evaluation of the 1,5-Diarylpyrazole Class of Cyclooxygenase-2 Inhibitors: Identification of 4-[5-(4-Methylphenyl)-3-(trifluoromethyl)-1*H*-pyrazol-1-yl]benzenesulfonamide (SC-58635, Celecoxib), J. Med. Chem. 40 (1997) 1347–1365.

[32] H.-P. Guan, X.-Q. Tang, B.-H. Luo, C.-M. Hu, Convenient Synthesis of Fluoroalkyl-Substituted Heterocycles from 1-Fluoroalkyl-2-iodoalkenes, Synthesis (1997) 1489–1494.

[33] H.-B. Yu, W.-Y. Huang, A convenient synthesis of 3-polyfluoroalkyl pyrazoles and 6-polyfluoroalkyl pyrimidines from β-polyfluoroalkyl enaminones, J. Fluorine Chem. 84 (1997) 65–67.

[34] H.-B. Yu, W.-Y. Huang, A novel precursor for per(poly)fluoroalkyl heterocycles from *N*-aryl per(poly)fluoroalkyl imidoyl iodides, J. Fluorine Chem. 87 (1998) 69–73.

[35] H.G. Bonacorso, A.D. Wastowski, N. Zanatta, M.A.P. Martins, J.A. Naue, Haloacetylated enol ethers 10. Condensation of β-alkoxyvinyl trifluoromethyl ketones with thiosemicarbazide. Synthesis of new trifluoromethyl 4,5-dihydro-1*H*-1-pyrazolethiocarboxyamides, J. Fluorine Chem. 92 (1998) 23–26.

[36] S.P. Singh, D. Kumar, B.G. Jones, M.D. Threadgill, Formation and dehydration of a series of 5-hydroxy-5-trifluoromethyl-4,5-dihydropyrazoles, J. Fluorine Chem. 94 (1999) 199–203.

[37] F. Foti, G. Grassi, F. Risitano, First synthesis of a bromonitrilimine. Direct formation of 3-bromopyrazole derivatives, Tetrahedron Lett. 40 (1999) 2605–2606.

[38] L.-p. Song, S.-Z. Zhu, Regioselective synthesis of fluorinated pyrazole derivatives from trifluoromethyl-1,3-diketone, J. Fluorine Chem. 111 (2001) 201–205.

[39] I.H. Jeong, S.L. Jeon, Y.K. Min, B.T. Kim, A novel approach to β-trifluoromethyl enaminones, Tetrahedron Lett. 43 (2002) 7171–7174.

[40] V.K. Aggarwal, J. Vicente, R.V. Bonnert, A Novel One-Pot Method for the Preparation of Pyrazoles by 1,3-Dipolar Cycloadditions of Diazo Compounds Generated in Situ, J. Org. Chem. 68 (2003) 5381–5383.

[41] D.N. Moreira, C.P. Frizzo, K. Longhi, N. Zanatta, H.G. Bonacorso, M.A.P. Martins, An efficient synthesis of 1-cyanoacetyl-5-halomethyl-4,5-dihydro-1*H*-pyrazoles in ionic liquid, Monatsh. Chem. 139 (2008) 1049–1054.

[42] M.A.P. Martins, D.N. Moreira, C.P. Frizzo, P.T. Campos, K. Longhi, M.R.B. Marzari, N. Zanatta, H.G. Bonacorso, X-ray structure, semi-empirical MO calculations and π-electron delocalization of 1-cyanoacetyl-5-trifluoromethyl-5-hydroxy-4,5-dihydro-1*H*-pyrazoles, J. Mol. Struct. 969 (2010) 111–119.

[43] M.A. Spackman, J.J. McKinnon, Fingerprinting intermolecular interactions in molecular crystals, CrystEngComm 4 (2002) 378–392.

[44] M.A. Spackman, D. Jayatilaka, Hirshfeld surface analysis, CrystEngComm 11 (2009) 19–32.

[45] C. Jelsch, K. Ejsmont, L. Huder, The enrichment ratio of atomic contacts in crystals, an indicator derived from the Hirshfeld surface analysis, IUCrJ 1 (2014) 119–128.

[46] P.R. Spackman, M.J. Turner, J.J. McKinnon, S.K. Wolff, D.J. Grimwood, D. Jayatilaka, M.A. Spackman, CrystalExplorer: a program for Hirshfeld surface analysis, visualization and quantitative analysis of molecular crystals, J. Appl. Crystallogr. 54 (2021) 1006–1011.

[47] R. Krishnan, J.S. Binkley, R. Seeger, J.A. Pople, Self-consistent molecular orbital methods. XX. A basis set for correlated wave functions, J. Chem. Phys. 72 (1980) 650–654.

[48] A.D. Becke, Density-functional thermochemistry. III. The role of exact exchange, J. Chem. Phys. 98 (1993) 5648–5652.

[49] M.J. Frisch, J.A. Pople, J.S. Binkley, Self-consistent molecular orbital methods 25. Supplementary functions for Gaussian basis sets, J. Chem. Phys. 80 (1984) 3265–3269.

[50] R. Dennington, T.A. Keith, J.M. Millam, GaussView, Version 6.0, Semichem Inc., Shawnee Mission, KS (2016).

[51] M.J. Frisch, G.W. Trucks, H.B. Schlegel, G.E. Scuseria, M.A. Robb, J.R. Cheeseman, G. Scalmani, V. Barone, B. Mennucci, G.A. Petersson, H. Nakatsuji, M. Caricato, X. Li, H.P. Hratchian, A.F. Izmaylov, J. Bloino, G. Zheng, J.L. Sonnenberg, M. Hada, M. Ehara, K. Toyota, R. Fukuda, J. Hasegawa, M. Ishida, T. Nakajima, Y. Honda, O. Kitao, H. Nakai, T. Vreven, J.A. Montgomery Jr., J.E. Peralta, F. Ogliaro, M. Bearpark, J.J. Heyd, E. Brothers, K.N. Kudin, V.N. Staroverov, T. Keith, R. Kobayashi, J. Normand, K. Raghavachari, A. Rendell, J.C. Burant, S.S. Iyengar, J. Tomasi, M. Cossi, N. Rega, J.M. Millam, M. Klene, J.E. Knox, J.B. Cross, V. Bakken, C. Adamo, J. Jaramillo, R. Gomperts, R.E. Stratmann, O. Yazyev, A.J. Austin, R. Cammi, C. Pomelli, J.W. Ochterski, R.L. Martin, K. Morokuma, V.G. Zakrzewski, G. A. Voth, P. Salvador, J.J. Dannenberg, S. Dapprich, A.D. Daniels, O. Farkas, J.B. Foresman, J.V. Ortiz, J. Cioslowski, D.J. Fox, Gaussian 09, Revision D.01 (2013).

[52] R.F.W. Bader, A quantum theory of molecular structure and its applications, Chem. Rev. 91 (1991) 893–928.

[53] J. Contreras-Garcia, E.R. Johnson, S. Keinan, R. Chaudret, J.-P. Piquemal, D. N. Beratan, W. Yang, NCIPLOT: A Program for Plotting Noncovalent Interaction Regions, J. Chem. Theory Comput. 7 (2011) 625–632.

[54] T. Lu, F. Chen, Multiwfn: A Multifunctional Wavefunction Analyzer, J. Comput. Chem. 33 (2012) 580–592.

[55] W. Humphrey, A. Dalke, K. Schulten, VMD: visual moleculardynamics, J. Mol. Graph. 14 (1996) 33–38.

[56] J. Racine, gnuplot 4.0: A portable interactive plotting utility. (2006) WileyOnline Library.

[57] https://cadd.labshare.cn/cb-dock2/php/index.php.

[58] Y. Liu, X. Yang, J. Gan, S. Chen, Z.-X. Xiao, Y. Cao, CB-Dock2: improved protein–ligand blind docking by integrating cavity detection, docking and homologous template fitting, Nucleic Acids Res. 50 (2022) W159–W164.

[59] J. Eberhardt, D. Santos-Martins, A.F. Tillack, S. Forli, AutoDock Vina 1.2.0: New Docking Methods, Expanded Force Field, and Python Bindings, J. Chem. Inf. Modeling 61 (2021) 3891–3898.

[60] Y. Rose, J.M. Duarte, R. Lowe, J. Segura, C. Bi, C. Bhikadiya, L. Chen, A.S. Rose, S. Bittrich, S.K. Burley, J.D. Westbrook, RCSB protein data bank: Architectural advances towards integrated searching and efficient access to macromolecular structure data from the PDB archive, J. Mol. Biol. 433 (2021) 166704.

[61] Accelrys Software Inc, Discovery Studio Modeling Environment; Release 3.5; Accelrys Software Inc, San Diego, CA, USA, 2013.

[62] A. Daina, O. Michielin, V. Zoete, SwissADME: a free web tool to evaluate pharmacokinetics, drug-likeness and medicinal chemistry friendliness of small molecules, Sci. Rep. 7 (2017) 42717.

[63] P. Banerjee, E. Kemmler, M. Dunkel, R. Preissner, ProTox 3.0: a webserver for the prediction of toxicity of chemicals, Nucleic Acids Res. 52 (2024) W513–W520.

[64] https://tox.charite.de/protox3/.

[65] G.M. Sheldrick, *SHELXT* – Integrated space-group and crystal-structure determination, Acta Cryst A71 (2015) 3–8.

[66] C.F. Mackenzie, P.R. Spackman, D. Jayatilaka, M.A. Spackman, CrystalExplorer model energies and energy frameworks: extension to metal coordination compounds, organic salts, solvates and open-shell systems, IUCrJ 4 (2017) 575–587.

[67] P. Pérez, L.R. Domingo, A. Aizman, R. Contreras, Chapter 9 The electrophilicity index in organic chemistry, in: Theoretical and Computational Chemistry; Ed. A. Toro-Labbé, 19, Elsevier B.V., 2007, pp. 139–291.

[68] B.S. Abdulrahman, R.B. Nadr, R.A. Omer, Y.H. Azeez, R.O. Kareem, D.A. Safin, Synthesis, characterization and computational studies of a series of the thiazole-thiazolidinone hybrids, J. Mol. Struct. 1324 (2025) 140806.

[69] M. Li, Q. Luo, Y. Tao, X. Sun, C. Liu, Pharmacotherapies for drug-induced liver injury: a current literature review, Front. Pharmacol. 12 (2022) 806249.

[70] G.R. Serjeant, The emerging understanding of sickle cell disease, Br. J. Haematol. 112 (2001) 3–18.

[71] C.K. Tebbi, Sickle Cell Disease, a Review. Hemato 3 (2022) 341–366.

[72] WHO. Sickle Cell Disease. Available online: https://www.afro.who.int/health-topics/sickle-cell-disease (accessed on 15 January 2025).

[73] E. Gonçalves, S. Smaoui, M. Brito, J.M. Oliveira, A.P. Arez, L. Tavares, Sickle Cell Disease: Current Drug Treatments and Functional Foods with Therapeutic Potential, Curr. Issues Mol. Biol. 46 (2024) 5845–5865.

[74] C.H. Reynolds, B.A. Tounge, S.D. Bembenek, Ligand Binding Efficiency: Trends, Physical Basis, and Implications, J. Med. Chem. 51 (2008) 2432–2438.

[75] S. Schultes, C. de Graaf, E.E. haaksma, I.J.P. de Esch, R. Leurs, O. Krämer, Ligand efficiency as a guide in fragment hit selection and optimization, Drug Discovery Today: Technol 7 (2010) e157–e162.

[76] J.P. Hughes, S. Rees, S.B. Kalindjian, K.L. Philpott, Principles of early drug discovery, Br. J. Pharmaco. 162 (2011) 1239–1249.

[77] A.L. Hopkins, G.M. Keserü, P.D. Leeson, D.C. Rees, C.H. Reynolds, The role of ligands efficiency metrics in drug discovery, Nat. Rev. Drug Discov. 13 (2014) 105–121.

[78] M. Abdul-Hammed, I.O. Adedotun, V.A. Falade, A.J. Adepoju, S.B. Olasupo, M.W. Akinboade, Target-based drug discovery, ADMET profiling and bioactivity studies of antibiotics as potential inhibitors of SARS-CoV-2 main protease (Mpro), VirusDis 32 (2021) 642–656.

[79] https://www.molinspiration.com/services/logp.html.